Instrumented tests on composite pressure vessels (type IV) under internal water pressure

Eric Lainé, Jean-Christophe Dupré, Jean-Claude Grandidier, Maxime Cruz

Instrumented tests on composite pressure vessels (type IV) under internal water pressure

Eric Lainé[1], Jean-Christophe Dupré[2], Jean-Claude Grandidier[1], Maxime Cruz[1]

[1]Institut Pprime, UPR3346 CNRS, ISAE-ENSMA, Université de Poitiers, ISAE-ENSMA - Téléport2 - 1 Av. Clément Ader - BP40109, F-86962 Futuroscope Chasseneuil Cedex

[2]Institut Pprime, UPR3346 CNRS, Université de Poitiers, ISAE-ENSMA, SP2MI - Téléport2 - Bd Marie et Pierre Curie - BP30179, F-86962 Futuroscope Chasseneuil Cedex

*corresponding author:
Eric Lainé
Institut Pprime, Department of Physics and Mechanics of Materials
1 avenue Clément Ader - BP40109- 86961 Chasseneuil Futuroscope, France
Tel: + 33-549-498222
Fax: +33-549-498238
e-mail: eric.laine@ensma.fr

Abstract

Much work has already been done on Type IV high-pressure vessels, both from an experimental and numerical point of view. The prediction of the maximum pressure before bursting, the effect of thermal cycles, defect and damage tolerance, fire resistance, liner collapse are topics generally numerically studied at the scale of the samples. In these previous works, the passage from the specimen to the structure is not fully validated by comparing the models with experimental measurements at the scale of the tank. However, this correlation with numerical simulation requires collecting a large amount of information, often by combining several metrological studies. In this work, non-destructive instrumented tests on a vessel subjected to internal pressure were performed coupled with optical measurements (3D displacement fields) and acoustic emission to understand the damage kinetics. Three load-unload tests are performed at speeds of 1, 10, and 100MPa/min up to 87.5MPa pressure, followed by a cyclic test (160 cycles). The results obtained show the interest of coupling field measurements with acoustic emission to evaluate the behavior of the pressure vessels and compare them with numerical models.

Keywords
HP tank-type IV, mechanical tests, internal pressure, optical measurements, acoustic emission

1 Introduction

Composite pressure tanks are now a mature way of storing compressed hydrogen. The combination of low weight and high mechanical strength made them particularly suitable for applications requiring large quantities of gas in a reduced and transportable volume, such as automotive fuel tanks or gas transport trailers [1]. This study focuses on a high-pressure type IV (hydrogen) tank consisting of an inner shell called a polymer liner on which the carbon fibers impregnated with a thermosetting resin are wound. The mechanical resistance is ensured by the

composite, the liner ensuring a large part of the gas tightness. Much work has already been done on these vessels, both from an experimental and a numerical point of view. The prediction of maximum pressure before bursting [2], the effect of thermal cycles [3-7], defect and damage tolerance [8-11], fire resistance [12], liner collapse [13-14] are themes generally studied at the sample scale and numerically. Over the last two decades, experimental and/or numerical studies [2,7,15-28] on pressure vessels have been carried out to understand their behavior under different mechanisms (burst, under fire, damage, …). In these previous studies, the passage from the specimen to the structure is not fully validated by a comparison of the models with experimental measurements at the scale of the vessel. It is important to remark that experimental tests instrumented on structures such as vessels are not always performed due to the cost and complexity of the experimental program. It is not always possible to test a vessel geometry (2.4-L, 19L, 36L...) under all conditions required by the specifications. Therefore, it is necessary to validate some modeling approaches that can reliably simulate experimental data and predict the performance of other cylinder types.

However, a correlation with numerical simulation requires a large amount of information to be collected by combining metrology such as surface field measurement at the tank scale and analysis by acoustic emission. Knapp et al. [18] developed a new concept for monitoring the structural integrity of filament-wood pressure vessels using an optical sensor. Degrieck et al. [19] embedded an optical fiber Bragg sensor into a carbon/epoxy filament-wound pressure vessel to monitor strain and temperature signals. Walker et al [20] predicted neural network burst pressure and acoustic emission for impact-damaged composite pressure vessels. Yao et al. [21] studied the deformation measurement of composite pressure vessels using a 2D digital image correlation (DIC) method in a composite pressure vessel under internal pressure. They validated their strain results by comparing them with measurements from conventional electronic strain gauge technology. Then in the same context, Meng et al. [22] extended their work to the 3D deformation in the field of a carbon fiber/epoxy composite pressure vessel is studied using a 3D numerical correlation method of the speckle. More recently, Gasior et al. [23] presented a methodology for displacement and strain measurements in composite storage tanks for hydrogen and high-pressure methane type IV in the areas of the gaseous fuel cell vehicle. Their work was carried out in vessels with so-called programmed defects in the form of notches and delamination. The complementary optical methods, namely: fiber optic detection based on Bragg gratings (FBG) and digital image correlation (DIC) was used to perform local and full-field displacement and strain measurements respectively. Gasior et al. [23] demonstrated that DIC can be successfully applied as a method of identifying defects in the field of view and that it can support optimal location and calibration of FBG sensors. As FBG sensors are intended to be integrated into the tank structure, the proposed methodology is a solution to the difficult problem of building an effective structural health monitoring system (SHM) for high-pressure composite gas fuel tanks. For field measurement, a 2D measurement (DIC [29,30] or marker tracking [29,31]) is not suitable because the vessel is not planar. The mechanical displacement field is 3D on a curved structure with a generalized swelling of this one. This is why a marks stereoscopic technique, which makes it possible to obtain the 3D displacements on the surface of a structure of any shape [29,31,32] has been retained. This late provides surface displacements and strains at particular points that can be directly matched to the mesh used for numerical simulations.

Acoustic emission has become an important non-destructive evaluation (NDE) technique in structures working under the gas or liquid pressure [24-28]. The use of acoustic emission (AE)

for damage detection in carbon fiber composite pressure vessels has been evaluated for the constant and cyclic internal pressure loading conditions of the gas [13]. On specimens, the EA technique can detect the initiation and accumulation of damaging events, and it is possible to reliably distinguish carbon fiber failure at other microscopic damage events [33-35]. In the case of structures such as a tank, it is more complex because many factors can disrupt the measurements. Thus, the AE method was used to explore thermomechanical properties under hydraulic and atmospheric fatigue cycles [25], to detect damage caused by the constant and cyclic internal pressure loading of the gas [26], to evaluate the state of damage during the hydrogen filling process [27] in type IV hydrogen composite pressure vessels. However, these studies did not characterize the damage modes and recognize the damage evolution mechanisms on the composite vessels. More recently, Liao et al. [28] have characterized the damage mechanisms of 70MPa type IV hydrogen composite pressure vessels during the 0–105MPa and 0–158MPa hydraulic tests of two vessels using the multi-step loading method. The authors used a multi-parameter statistical analysis method (MPSA) based on empirical decomposition (EMD) and the *K*-means algorithm is performed to cluster AE events for the vessels. Finally, they show that the AE method can be reliably used to characterize the mechanisms of damage evolution in composite pressure vessels.

Although the damage to these structures has been studied, the basic question of the cyclic behavior of the tank in conventional use has been asked too little. Do hysteresis phenomena occur? Accumulations of residual deformations can appear? Such accumulations can generate a modification of the long-term stress fields after a large number of cycles? The evolutions of damage mechanisms under variable use pressure are essential to identify and characterize to study durability. A reference must be built to then be able to study the deviations from it in extreme configurations such as impact, bursting, and strong temperature variations.

This means being able to carry out load-unload and cyclic pressure tests with a large number of cycles while ensuring the continuity of metrology. In this paper, the behavioral model used in numerical simulation is basic it has been chosen to show that experimental and numerical comparison is feasible and demonstrates the possibilities provided by the test.

In addition to what has already been done and is found in the literature, the originality of this study is twofold:

- Couple acoustic and stereoscopic emission techniques to characterize the first mechanisms of a Type IV composite pressure vessel used for the storage of hydrogen under 87.5MPa water pressure,
- Assess the feasibility, interest, and relevance of acoustic and optical measurements to understand the increase in the knowledge of vessels during a cyclic (long time) test.

In this work, non-destructive instrumented tests on a high-pressure vessel subjected to internal water pressure coupled with optical measurements (3D displacement fields) and acoustic emission are carried out. Measurements were made on a single tank subjected to a static charge at three different loading speeds and a cyclic test (160 cycles). Paragraph 2 presents the type IV high-pressure tank used for the study. The experimental system, the optical measurement method (3D displacement fields), and the acoustic emission technique are detailed in paragraph 3. Paragraph 4 sets out the results of the loading-unloading tests carried out at rates of 1, 10, and 100MPa/min up to a pressure of 87.5MPa and a cycling test. The results of acoustic measurements are discussed and those of optical measurements are correlated with FEA results.

2 Experimental structure

The pressure vessel (Figure 1) used for this work was specially manufactured for R&D project purposes and is not currently available on the market. It is part of a batch of 12 manufactured specifically for the program project (COLLINE) and very similar to #05 presented in [17]. It has been designed according to the standards for transportable cylinders [36], i.e. aiming for burst pressure of 3 times the working pressure of 70MPa. It has an internal volume of 2.4-L. The ratio of thickness to external diameter (t/D) of the bottle is 0.019. Before this test campaign, this tank was used as part of the COLLINE project where it was subjected to a rapid hydrogen decompression test. It was pressurized to 70MPa and then emptied at 0.07MPa/min to atmospheric pressure.

In [17], it was specified that three of the twelve cylinders used were also Xray-CT scanned before testing to provide the initial state. Thus, even though the pressure vessels have been submitted to nothing else than a hydraulic proof test just after manufacturing (ca. 30s hold at 105MPa hydraulic pressure - a mandatory step to ensure safety). The authors observed that out of the three, there were areas with a small gap between the liner and the composite (Figure 1a). The reasons have not been identified but two hypotheses have been proposed: whether it is due to the manufacturing process, with a winding made before the polymer has finished shrinking, or due to hydraulic proof test. Anyway, this initial state must be taken into account when analyzing the post-decompression state. After the decompression test at 0.07MPa/min., this vessel has gaps between the liner and composite seem to be a bit more marked than in the initial state. As the Xray-CT scan is performed after one week, the gap has disappeared and the coating is in full contact with the composite, the interface has not been reconstructed but the shape of the coating has adapted itself (Figure 1b).

Figure 1: Tomography of the high-pressure tank H_2 type IV (a) before tests – (b) after the static and cyclic tests.

3 Experimental

3.1 Experimental method(ENDOMAT)

The Endomat experimental test bench (Figure 2a) uses a tri-axial mechanical test machine to carry out tensile-compression, torsion, and torsion tests coupled or not to internal pressure. The limit values of the machine are 1200kN in tensile-compression, 55kNm in torsion, and 120MPa in the pressure test. The dimensions of the test machine allow large structures to be fixed on the test bench. The three load axes impose static and dynamic loads, possibly synchronized, over a frequency range up to 10Hz depending on the amplitude of the controlled forces. In this work, only pressure loading is used.

The pressure axis has two devices in parallel, combining the hydraulic power in oil with the hydraulic circuit in water injected into the structure to be tested. The combination of two transfer accumulators (oil/water) transfers the pressure supplied by the circuit into the oil using bladders (operating pressure of the hydraulic units: 30MPa). The pressure transfer ratio is then 1 but this system has the advantage of being able to provide high flow rates (movable volume: 24L; pilot servo valve flow rates: 520L/min and 75L/min) responding to the problems of structures undergoing large deformations. The second device is a suppressor that multiplies the

pressure by 4 thanks to the sections of the piston. The system can convert the operating pressure to oil from 30MPa at a pressure of 120MPa in the water circuit but for a lower flow rate (Displaceable volume: 5L; servo pilot valve flow rate: 20L/min). The test bench is composed of DOLI control electronics.

In their current use, the hydrogen tanks are under pneumatic loading, whereas here the tests are under hydraulic loading. For the stresses generated, the differences between these two types of loading can only come from the couplings created by diffusion. However, hydrogen generates very little volume when dissolved in the liner or the composite and does not affect the behavior of the materials. In the time of the experiments (cycling), water only reaches a very small thickness of the liner. Therefore, it is reasonable to assume that the two mechanical loads are similar. Obviously, in a pneumatic filling or emptying phase, the temperatures do not evolve in the same way as in the underwater experiments. This is a point that would require a specific study.

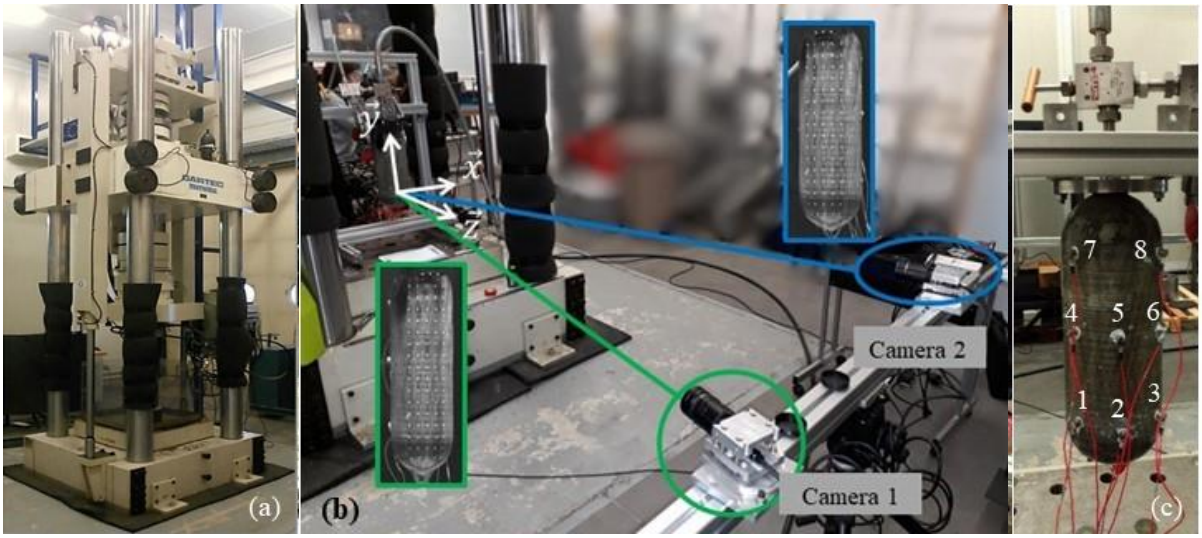

Figure 2: (a) ENDOMAT – (b) Tank side optical measurements – (c) Tank side acoustic emission sensors

3.2 Optical measurement and analysis

The measurement is based on a stereoscopic vision to obtain the evolution of the surface positions of the specimen in the space. Two techniques developed in the laboratory can be used: the mark tracking technique and the digital image correlation. To compare with the finite element approach, the marks tracking method is chosen. It allows us to directly associate experimental marks and digital nods. It consists of plotting a series of dots on the surface of the tank using a regular grid (stencil) with a 20mm pitch between each marker horizontally and vertically.

The analysis is done thanks to two digital cameras (cameras 1 and 2) (Figure 2.b). [29,32] Each camera record simultaneously an image of the surface. Home-made software is used. The first step is to calculate the coordinates $\bar{X}_{C1}$ and $\bar{X}_{C2}$ of each marks in the coordinate system of each camera. It is similar to calculating a centroid, the equation is of the form [31]:

$$\bar{\boldsymbol{X}}_{\boldsymbol{C}} = \begin{bmatrix} \frac{\sum_i x_i (I_i - I_s)}{\sum_i (I_i - I_s)} \\ \frac{\sum_i y_i (I_i - I_s)}{\sum_i (I_i - I_s)} \end{bmatrix} \quad (1)$$

with I_i is the intensity of the pixel with i the index of coordinates (x_i, y_i). These coordinates are limited to a subset previously defined. I_s is the intensity level of the studied subset to define whether a pixel belongs to the markers or is a part of the image background. This intensity threshold can be modulated during the test for example, depending on the average of values in the subset.

The second step is the triangulation process; it consists of calculating the 3D coordinates $\bar{X}_R$ of the marks by:

$$\begin{cases} \bar{\bar{R}}_1 \, \bar{X}_R = \bar{\bar{G}}_1 \, \bar{X}_{C1} \\ \bar{\bar{R}}_2 \, \bar{X}_R = \bar{\bar{G}}_2 \, \bar{X}_{C2} \end{cases} \tag{2}$$

where $\bar{X}_{C1}$ and $\bar{X}_{C2}$ are the coordinates of the markers in the reference frame of both cameras. The position of the cameras are defined by $\bar{\bar{R}}_1$, $\bar{\bar{R}}_2$ a rotation matrix (angular positions of the cameras: α_1, α_2 around $\vec{y}$ and β_1, β_2 rotation around $\vec{x}$) and. $\bar{\bar{G}}_1$, $\bar{\bar{G}}_2$ a transformation matrix (γ_1, γ_2 the magnificent and L_1, L_2 the distances between the cameras and the origin of the referential) (Figure 3a).

A preliminary step of calibration is necessary to obtain rotation and transformation matrix. It consists to solve formula (2) with the help of data obtained from images of a grid of marks with known positions of dots.

The variation of the $\bar{X}_R$ coordinates during the loading allow us to obtain the displacements vector of each mark and the strain field. The procedure provides the positions of the spots in each mechanical state of the specimen. Through the difference of positions between two loading states, can be calculated the displacement of each spot $\underline{U}$ in the (x,y,z) referential or cylindrical referential to analyze the radial and axial displacements (3):

$$\underline{U} \begin{cases} U_x(x,y,z(x,y)) \\ U_y(x,y,z(x,y)) \\ U_z(x,y,z(x,y)) \end{cases} \; or \; \begin{cases} \sqrt{(U_x(x,y,z(x,y)))^2 + (U_z(x,y,z(x,y)))^2} \\ U_y(x,y,z(x,y)) \end{cases} \tag{3}$$

Strains are calculated by finite differences from 4 markers defining a square with the assumption of local plane surface (Figure 3-b). Two vectors (dX_1, dX_2) in the initial state and two vectors in the deformed state (dx_1, dx_2) are defined. For each loading step, the normal to the surface locally defined by the markers is calculated. It gives two angles (α, β) defining the orientation of the normal both in the initial state and the deformed state.

(a) Calibration parameters

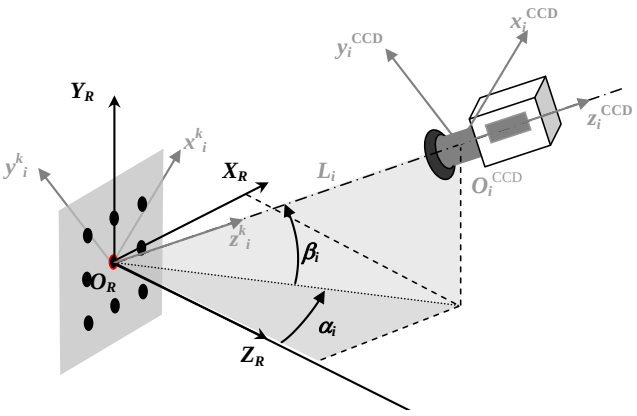

(b) Strain calculation

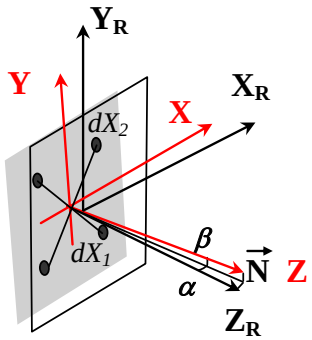

Figure 3: Parameters for the calibration process (a) and strain calculation (initial state) (b)

Gradient tensor of the transformation $\bar{\bar{F}}$ [29,31] can be calculated by solving the system:

$$\underline{dx_i} = \bar{\bar{F}}\underline{dX_i} \tag{4}$$

with i = 1,2 and $$\bar{\bar{F}} = \begin{bmatrix} F_{XX} & F_{XY} & 0 \\ F_{YX} & F_{YY} & 0 \\ F_{ZX} & F_{ZY} & 0 \end{bmatrix} \tag{5}$$

Then the Green-Lagrange tensor representing the lagrangian strains in the space (XYZ) is [29]:

$$\bar{\bar{E}} = \frac{1}{2}(\bar{\bar{F}}^T\bar{\bar{F}} - \bar{\bar{I}}). \tag{6}$$

The uncertainty has been assessed by a displacement test of the grid used for calibration. The bias error between imposed and measured displacement allows calculating a standard deviation equal to 9/1000mm in x and y direction and 2/100mm in the z-direction (out of plan), which gives with an interval of confidence of 95% uncertainties of 2/100mm and 4/100mm respectively. In terms of strain, the uncertainty obtained is 0.01%.

3.3 Acoustic emission for structural and analytical tests

Damage control is carried out by measuring acoustic emissions. An 8-channel Mistras Group 8-channel express system is used to record AE signals on the tank. All tests are performed with eight acoustic piezoelectric sensors with a PAC 1220A preamplifier with a gain of 40dB. They are positioned on the tank with silicone grease and fixed with adhesive tape (Figure 2c). The sensors are positioned on 1/3 of the cylinder perimeter (120°) and a height corresponding to the cylindrical part of the tank. Sensors 1, 2, and 3 are placed at the intersection between the cylindrical part and the lower dome; sensors 4.5 and in the middle of the height of the cylindrical part and sensors 7 and 8 at the intersection between the cylindrical part and the upper dome (Figure 2c). When recording AE signals, a detection threshold (32dB) is selected below which no signal is recorded. Signal propagation is evaluated by the mine failure procedure [37-38]. Time-dependent parameters, such as amplitude, energy, duration, rise time, number of counts, etc. are calculated in real-time by the acquisition system. Directly related to waveform shape, these characteristics are widely used for AE analysis. Besides, the acquisition is synchronized with the internal pressure applied to the tank (signal 0-10V).

The first analysis that can be done during an acoustic emission test is to represent all the recorded signals in the form of amplitude - number of counts. In this representation, signals with a small amplitude and many points corresponding to mechanical noise are eliminated, as well as those with a large amplitude and a small number of points corresponding to electromagnetic noise [33]. Secondly, it is not easy to process the different parameters of AE signals, especially when the structure is complex, such as the tank due to its geometry and the stacking of a large number of folds with very different orientations. There are different approaches in the literature. Many studies have attempted to develop methods to differentiate the source mechanisms of acoustic emission signals by using a single parameter extracted from the waveform. While it appears that, based on the amplitude of the acoustic emission signals, it is possible to classify the most frequent damage modes encountered in composites (matrix cracking, delamination, and fiber breakage), it is nevertheless difficult to define precise limits

(in amplitude) for the damaged areas. These values may vary according to the material, the type of test... More recent work has shown that a parametric analysis of AE signals, using the amplitude, rise time, duration, and energy of the signals, can identify different types of signals called types A, B, C, and D [34-35] to classify the mechanisms. In the following, the type A, B, and C signals to be discussed will be defined according to the same criteria of amplitude, duration, and energy. Type D signals were not detected in any of the tests.

3.4 Protocol

In this section, the two types of tests carried out to evaluate the feasibility of obtaining the behavior of the vessel under cyclic load (in time) via simultaneous optical and acoustic measurements are presented. The two tests are:

- static charge-discharge tests (pressure and depressurization) with two cycles and three different loading and unloading speeds: 1, 10, and 100MPa/min,
- one cyclic test.

First, a test with two identical cycles is conducted in three configurations of different loading/unloading rates. A cycle consists of a load, a stabilization level of 600s at 87.5MPa pressure, a return to zero pressure (unloading), and a level of 600s at zero pressure. It permits to mimic real utilization. Three configurations of loading-unloading rate (1, 10, and 100MPa/min) are carried out successively on the same pressure vessel. They are spaced a minimum of two hours apart. This last point is very important to take into account in the analysis of the results. A final cyclical test was carried out. It is composed of 160 imposed identical cycles. Each cycle is decomposed by pressurizing to 87.5MPa at a speed of 100MPa/min, then holding at this pressure for 2s, depressurizing at 100MPa/min, and holding at zero pressure for 2s.

3.5 Design, geometry, and finite element modeling

This section presents assumptions and data concerning the tank geometry, the behavior of the composite material, and boundary conditions. The 2.4-L reference vessel is very close to the one studied experimentally and numerically by FEA (ABAQUS® software) as part of the characterization of the degradation of reservoirs subjected to shocks [38]. It is recalled that the type IV pressure vessels are obtained by the filament winding process over a polymer liner and metallic boss at the end. In addition to the geometry of the boss and of the liner, the finite element computations require the complete stacking sequence of the wound composite shell in the cylindrical part of the vessel, i.e. for each layer, the winding angle (measured concerning the tank axis) and the thickness. Due to the confidentiality of the industrial process, the exact lay-up is not disclosed in this paper. Figure 4a shows a representation of the lay-up: each color stands for a given angle. Note that because of the winding process, each layer is composed of two interlaced “sub-layers” ($+\theta$ and $-\theta$, where θ is the layer angle).

Three different materials are used in this container: steel, polyethylene, and carbon/epoxy composite for the boss, liner, and composite shell respectively. The mechanical behavior of polyethylene does not have a significant influence on the overall structure due to its low stiffness compared to composite or steel. Thus, for steel and polyethylene materials, classical elastic and plastic behaviors at ambient temperature have been used. The tabulated data have been entered into the model. The mechanical behavior of each sub-layer is considered as linear elastic and transversely isotropic. The materials data are confidential.

While the thickness and the angle of the layers remain constant in the cylinder, it is well known [39] that these geometric parameters evolve in the dome. Different theories explain these developments [40]. A simple and pragmatic approach was chosen here as in [16]: the thickness

and angle of each layer are assumed to be identical in the cylinder and the dome. Although this assumption is quite strong, it is assumed that the cylinder bursts in the central section and that the composite design at the dome does not have a major influence on the failure pressure.

The simulations take advantage of the symmetries of the problem: the geometry is axisymmetric (only a slice of the vessel is represented) and only one half of the tank is modeled (Figure 4a). This geometry has meshed with axisymmetric quadratic elements. Thanks to this geometrical assumption, the number of elements is limited and the computation time reduced (9963 elements for the boss and the liner, 28614 for the composite; the thickness of each composite layer contains one element).

The applied loading and boundary conditions are following the tests performed and presented below. Symmetry conditions are applied along the mirror plane (on the right-hand side of the geometry in Figure 4b). The metal boss is considered embedded in the threaded part, which allows the cylinder to be extended. A pressure (pink arrows on Figure 4b) is applied on the inner surface of the liner and the boss. The maximum pressure value that is applied during the tests is 87.5MPa, i.e. the working pressure.

Figure 4: 2.4-L tank (axisymmetric FE geometry) – (a) representation of the composite lay-up (the orange layer at the bottom is the liner) – (b) boundaries conditions, load

4 Results

4.1 Static load-unload tests at different pressure rates

Three static load-constant phase-unload tests (pressure and depressurization) with two cycles are performed on the same vessel. Only the loading and unloading rates are different: 1, 10, and 100MPa/min. The 87.5MPa and 0MPa steps have a duration of 10min for all three tests. The first important quantity to be exploited is the axial elongation of the tank. This is obtained by using a marker placed under the tank (Figure 5a, red dot). Figure 5b and Figure 5c show axial elongation and pressure vs. time (in minutes) and axial elongation vs. pressure respectively for the three static tests. These two figures show that in the first test with a speed of 1MPa/min, the maximum extension of the vessel is 0.80mm in the first cycle and 0.85mm in the second cycle. The response is perfectly linear without hysteresis. Thus, the response during depressurization of the first cycle is identical to that of the second cycle (loading and unloading). The results for the three tests are superimposed on each other both the loading and unloading phases.

To compare the experimental and numerical responses, Figure 5c superposes the numerical response to the experimental ones. Figure 5d shows relatively similar experimental responses of radial and axial displacement. The numerical response throughout the tank is close to the experimental ones. It is almost superimposed on the 1MPa/min test and is within the measurement ranges for the other two tests. On the other hand, while the axial elongation (Figure 5e) in the middle of the cylindrical part seems to be well numerically correlated, it is not the same over the whole height and in particular over the upper part. The hypotheses made in the description of the folds at the dome level mean that the displacements in the upper part of the tank are poorly described. On the other hand, in the lower part of the tank, the numerical response is closer to the experimental responses. With this measuring technique, it is possible to discern the effect of the orientation distribution of the fibers in the dome.

Figure 5f shows the experimental and numerical responses of the radial displacement of the horizontal generator located in the middle of the cylindrical part of the tank. The numerical response is constant since the numerical simulation was conducted on an axisymmetric model. As mentioned above, the error on the radial measurement (inflation) is higher than the axial measurement. Thus, we note that the numerical response is within the measurement intervals. The solid lines and the dotted lines in Figure 5f are drawn by linear regression. Except for the first test at 1MPa/min, note that for both tests (and cycles) these lines are almost horizontal. This reflects a homogeneity of the tank in the radial direction.

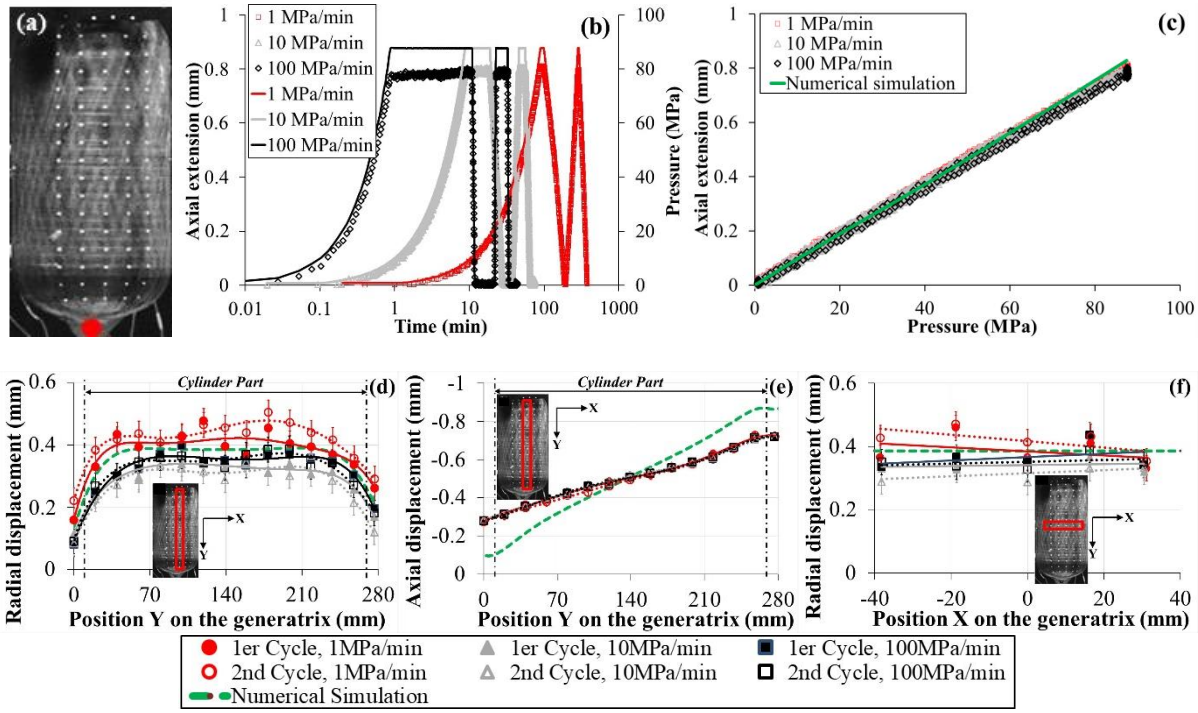

Figure 5: (a) Tank – (b) Axial extension (dots) and pressure (continuous line) versus time – (c) Axial extension versus pressure – (d) Radial displacement and (e) Axial displacement versus position markers on the generatrix Y – (f) Radial displacement versus position markers on the generatrix X, for all three pressure loading rates after each cycle

Figure 6a and Figure 6b present by example the maps of the measured radial and axial displacements fields (dR and dY) and deduced deformation fields for the maximum pressure (87.5MPa) during the second cycle of the 100MPa/min test. The radial displacement fields are slightly heterogeneous in the cylindrical part. However, the maximum values (about 0.40mm) are in the central part of the cylinder. There is a gradient of these displacements between the cylindrical part of the tank and the domes. In the axial direction, the displacement fields are distributed with a gradient over the whole height of the tank. In the cylindrical part of the tank, these displacements vary from 0.25 to 0.7mm. The radial (E11) and axial deformation (E22) fields are homogenous too in the cylindrical part with mean values of strain are 4.8 10^{-3} and of 1.8 10^{-3} respectively. On the other hand, Figure 6b shows larger axial deformations, in the order of 2 10^{-3}, located at the intersections between the cylindrical part and the domes. The vessel tomography presented in Figure 1a shows a decrease in vessel thickness in this area of between 18 and 24% compared to the thickness in the cylindrical part. This may justify a localized and higher axial strain field. Moreover, the variation in thickness (between 18 and 24%) seems to

be of the same order of magnitude as the variation in deformation between the cylindrical part and the intersection between the dome and the cylindrical part (about 25 to 30%).

Figure 7 shows the calculated fields by FEA. The field obtained by the numerical simulation is homogeneous for the radial displacement and linearly distributed longitudinally. In the axial direction, the displacement field is distributed with a slight "tilt" of the gradients. We note that the values are higher than the measured ones about 15%. (0.4 mm and 0.5mm for strain $5.5.10^{-3}$ and $2.3\ 10^{-3}$ respectively).

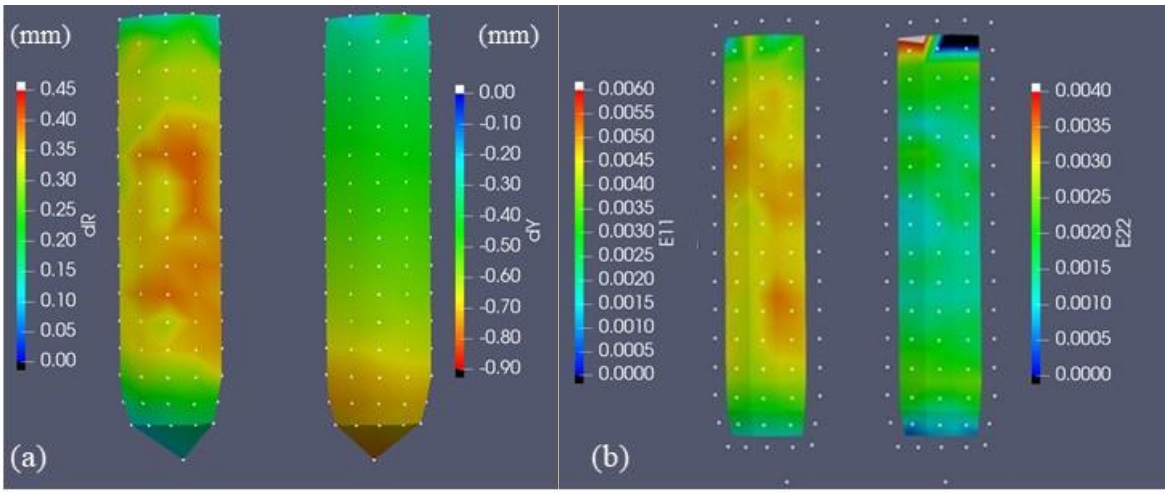

Figure 6: Test at 100MPa/min. Cycle 2 at maximum pressure (87.5MPa) – (a) Displacement (dR, dY) and (b) strain (E11, E22) fields by optical measurement

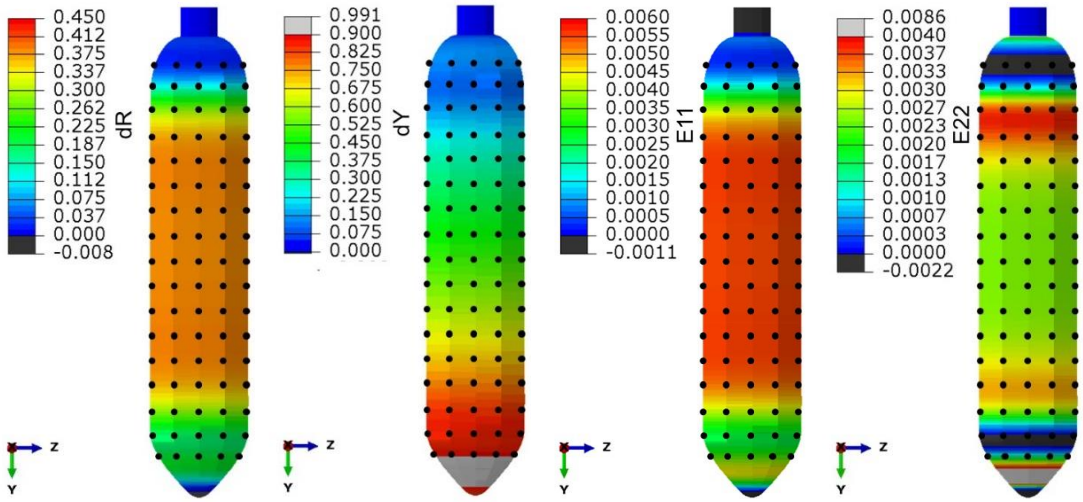

Figure 7: Radial (dR, E11) and axial (dY, E22) displacement (dR, dY) and strain (E11, E22) fields at maximum pressure (87.5MPa) by FEA

In view of the negligible effect of the loading speed on the various results and observable parameters, it is chosen for the following to present only the results for the test at 100MPa/min (Figures 8). During the test, AE is recorded continuous and Figure 8a shows the number of counts AE in a log scale (red and green squares for cycles 1 and 2 respectively) as a function of amplitude for the one loading rate and the two cycles imposed. In all three tests, the acoustic response is not affected by mechanical or electromagnetic noise. The signals are of the same nature for the three successive tests. The scale of amplitudes and the number of counts is identical, and the correlation is similar. These results are confirmed in figure 8a, where the

salves' number as a function of amplitude is represented. In the first test at 1MPa/min, a much higher number of pulses were observed in the first cycle and to a lesser extent in the second cycle. In contrast, in the next two tests (10 and 100MPa/min.), the acoustic signature was identical in the first and second cycles and very close to the second cycle of the 1MPa/min. test. During this first cycle, some particular events appeared, corresponding to the first adjustment of the structure. Noise cannot be excluded. Besides, the amplitudes vary mostly between 40 and 60dB. For the three tests, the proportion of hits between 40 and 60dB is about 98.5% of hits. There is an increase in activity during the loading phases, with the presence of the highest amplitude levels. There is an activity during periods of constant pressure and a stop during zero pressure phases.

Figure 8b illustrates the evolution of the cumulative number of AE signals for the test at 100MPa as a function of time. This cumulative number of AE signals is the sum of the signals detected by all the sensors during each cycle. In the first cycle at 1MPa/min., there are a large number of hits, more than twice as many as in the second cycle and the following tests. It appears during the first ramp of load and slows down very sharply during the first unloading without really canceling out. The acoustic activity during the second cycle of the first test is sharply reduced and it is closer to that measured during the cycles for 10 and 100MPa/min. tests. For 10 and 100MPa/min, the evolution is similar, but it is important to underlie, activity continues during the constant pressure phase and stop only when the pressure is null. This result suggests that the noise comes from internal surface friction or viscosity that changes under pressure. Stopping the acoustic emission under zero pressure with the blowers still running proves that the noise of the machine is of the second order.

Figure 8b shows the cumulative number of AE signals for each of the sensors. The position of the sensors and markers are shown in Figure 8c and superimposed on the strain field (E11, Figure 7) obtained by numerical simulation. For each sensor, there is an evolution following the results preceding a high activity during the first cycle of the first test and then an evolution which repeats itself with a similar acoustic signature for all zones. Thus, sensors 7 and 8 (Figure 2c, Figure 8c) are the ones that receive the most AE signals, approximately 1150 and 1650 respectively per cycle. Sensors 1, 2, and 3 placed at the intersection of the cylindrical part and the lower dome (Figure 2c, Figure 8c) pick up between 130 and 170 AE signals per cycle. Finally, sensors 4, 5, and 6 placed in the middle of the cylinder height have different acoustic responses, particularly the 4 and to a lesser extent the 5. At this stage, it is not possible to identify a particular reason but it can assume the source is mainly at the head of the tank where a metal/polymer/composite connection is subject to high stresses and relative movements can generate friction. Finally, it should be noted that if the first acoustic signals appear around 2MPa, the acoustic activity accelerates significantly from 50MPa (Figure 8b). The two sensors that receive the strongest signals are those close to the pressure supply and area of the grip of the tank, it cannot be excluded during the first phase that a large part of the acoustic emission comes from friction in the area of the connection with the machine and the pressure system, these two sources of noise being stopped in the phases of zero pressure. It is necessary to analyze the signals to conclude.

Figure 8d presents the acoustic response of the duration and absolute energy of AE signals as a function of amplitude. These three parameters combined define the areas defining Type A, B, and C signals. These areas are represented by black frames in this figure. The exploitation of these quantities [34-35] shows that the amplitude of the hits is between 40 and 70MPa (99.9%). Some signals are characterized by short-lived waveforms (less than 1ms) and relatively low energy. They could be similar to signals of type A [34], which are usually the

acoustic signature of matrix cracking. If the signals fall into this category, the time distribution correlating with the loading suggests that the emission is friction between elements. Is this friction at the level of the structure or at the level of the material (crack friction or viscosity) the question is open. The high activity at sensors 7 and 8 suggest friction in the head but the emission from the other sensors suggests composite liner friction and strong internal material friction.

Signals in the 70-100dB range could like to type B signals, as described in [34], and therefore correspond to fiber/matrix interfacial debonding. They represent only 0.1% of the acoustic signals received during the three tests. Finally, they generally appear each time during the second cycle. A third zone can be defined, here called zone C. The signals correspond to the activity observed during the first and second cycle, their durations (more than 1ms) are important with a low amplitude between 40 and 70dB. They undoubtedly correspond to the setting up of the test elements, but they are in the three tests carried out. In general, these durations appear at higher amplitudes (>70dB), which could confirm that the source of these signals is not due to the composite material.

Figure 8e illustrates the distribution of the number of signals and Figure 8f permits the temporal location of these signals. First, type A signals are distributed to all sensors. The distribution of these signals is the same for all three tests. These signals have a duration of less than 0.5ms during the loading ramp. The duration time starts to increase from 50MPa internal pressure. The number of these signals and their duration time increases during the constant plateau at 87.5MPa which lasts 10 minutes for each cycle and test. Almost all B and C signals appear at the constant plateau (87.5MPa). Although it is difficult to relate these signals to a damage mode, it seems that they are dependent on the speed of pressurization. Indeed, by observing. It appears that these signals shift in time. If the type C signals are distributed over the time of the 87.5MPa hold, the type C signals arrive almost at the same time. Moreover, their distribution is almost uniform and unitary on all the sensors except for the two placed at the top of the cylindrical part of the tank (sensors 7 and 8). These signals (B and C) can be the sign of a structural or friction effect in the assembly (liner/composite).

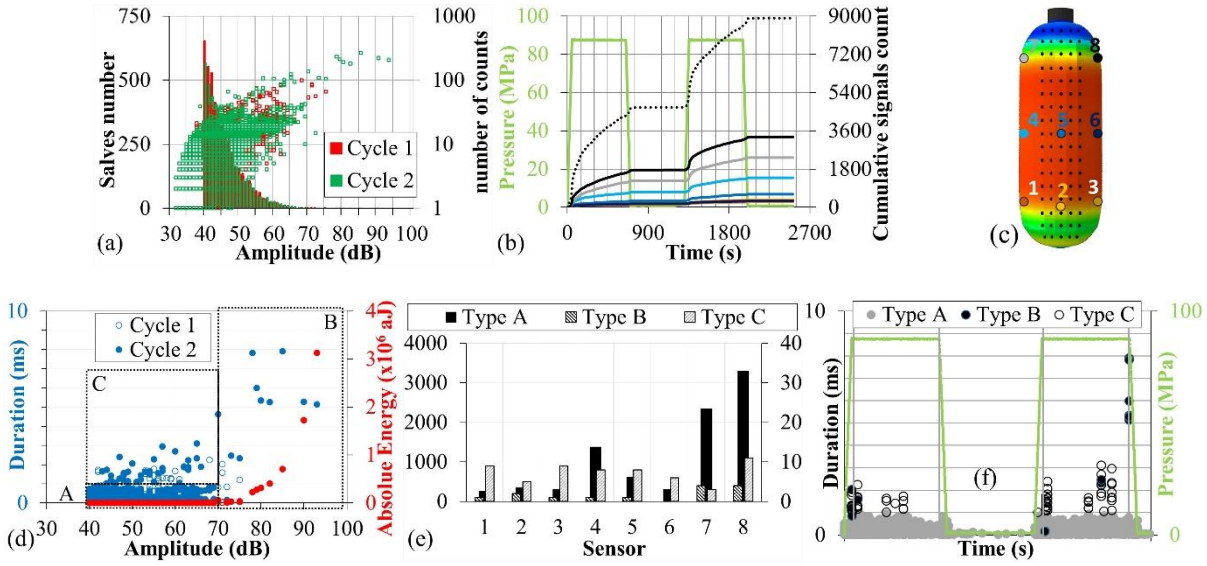

Figure 8: (a) Salves number and number of counts versus AE amplitude (dB) – (b) Individual acoustic response of the 8 EA sensors and the sum of the acoustic responses (black dotted line) - Cumulative number of AE signals and pressure versus time – (c) Location of EA sensors, markers on the E11 strain field obtained by numerical simulation – (d) Acoustic response of the

duration and absolute energy of AE signals as a function of amplitude – (e) Distribution of type A, B and C signals by sensors (The number of types A signals are counted via the left-hand scale from 0 to 400, types B and C via the right-hand scale from 0 to 40) – (f) Temporal location of type A, B and C signals during tests, for the test at 100MPa/min.

4.2 Cyclic test

A cyclic test of 160 triangular cycles (2s step between loads - unloads and unloads - loads) at a speed of 100MPa/min was performed after the three previous tests on the same tank. Each cycle lasts about 107s. Figure 9a shows the total extension of the vessel as a function of time during the cycling test. The elongation is almost stable, it oscillates between 0.795 and 0.80mm. Figure 9b presents the axial and radial displacements of the central marker located at the intersection of the horizontal (middle of the cylindrical part of the vessel) and vertical (middle of the observed cylindrical area) generatrices. Figure 9c plots the radial and axial strains in the first and last cycle at the same point. The axial and radial displacements of this marker are almost constant (such as the total elongation of the tank), these displacements are about 0.5 mm and 0.3mm respectively. The graphs in Figure 9 clearly show that there is no hysteresis effect on axial and radial displacements.

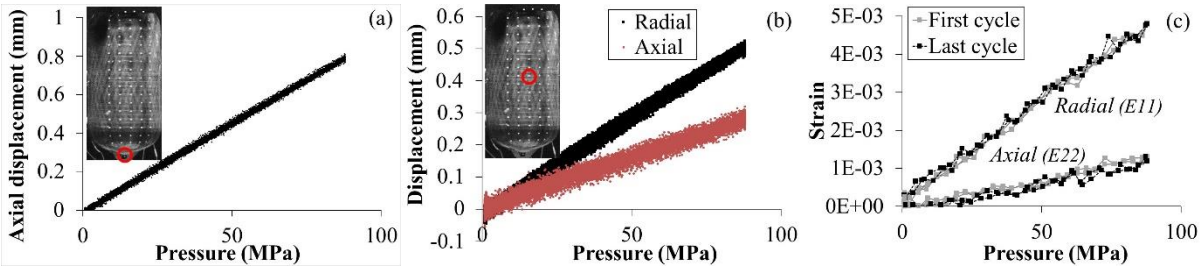

Figure 9: (a) Axial displacement versus pressure for the endpoint (circled in red) – (b) Axial and radial displacements versus pressure for the center point (circled in red) – (c) Axial and radial strains versus pressure for the center point (circled in red (b)) for the first and last cycle

By observing the maps of the radial and axial displacement fields of the first cycle 1, the eightieth, and the one hundred and sixtieth, it can be seen, as already mentioned, that there is no change over time in displacements. The values are about 1/10 of one mm smaller. Observation of the strain maps for the same cycles shows that the axial and circumferential deformations are constant.

Figure 10a, Figure 10b, and Figure 10c illustrate the cyclic test data set (i.e. 160 cycles), the number of counts as a function of AE amplitude, pressure, and amplitude as a function of time and the total number of hits per cycle, respectively. Figure 10a indicates during this cyclic test that the acoustic responses are not affected by either mechanical or electromagnetic noise. Figure 10b shows the pressure cycling curve (pale green) and the amplitude of the acoustic signals throughout the cyclic test. During some cycles, the acoustic signals were not perceived due to a technical problem. Therefore periods without signals appear in Figure 10b. Figure 10c depicts the number of hits per cycle. The line in black dashed corresponds to the linear regression considering all the points. If this line seems horizontal overall over all 160 cycles, there is nevertheless a decrease in hits per cycle between the fortieth and the one hundred and sixtieth cycles. The total measured amplitudes are between 40 and 60dB (99.95%).

Figure 11a describes the evolution of cumulative AE signals counts during the first, fortieth, eightieth, and one hundred and sixtieth cycles. Comparing activity in more detail in Cycles 1, 80, and 160, there is no change except for an increase in activity in the first cycle. However, it

is important to note that activity during the unloading phases is higher than during the loading phases, suggesting a 'non-material' origin of the emission. Figure 11b shows the acoustic response of the duration and absolute energy of the AE signals as a function of amplitude during the one hundred and sixtieth cycles. If some signals in the C-zone are present during the first cycle (at about 50MPa), Figure 11b shows that they hardly appear at cycle 160. Type B signals are almost non-existent in the acoustic response during this cycle test. Finally, Figure 11c presents the number of Type A signals per sensor during loading and unloading over one cycle for each of the three observed cycles (1, 80 to and 160). The distribution of Type A signals per sensor is almost identical to the previous tests. However, the number of signals per sensor decreases proportionally to the cycles during the pressure rise. On the other hand, the number of these signals increases in the unloading phase. Finally, the overall number of signals varies by only a few units between the first and one hundred and sixtieth cycle. These results confirm a friction mechanism that deploys at each load-unload phase. This friction is generalized to the whole bottle with an over-activity near the head.

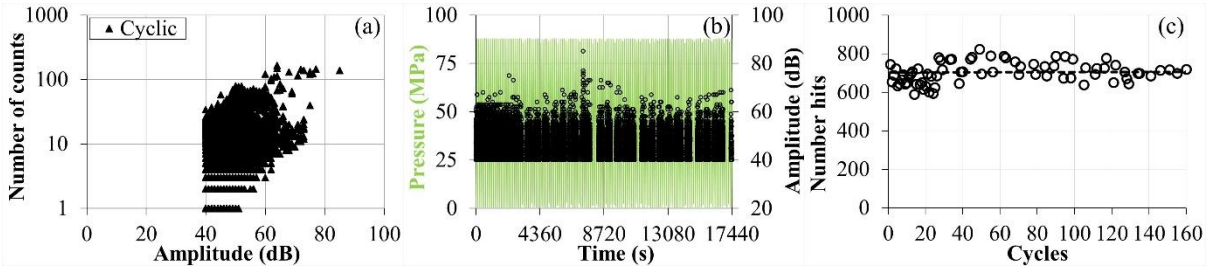

Figure 10: Cyclic test - (a) Number of counts versus AE amplitude (dB) – (b) Pressure and AE amplitude versus time – (c) number hits versus cycles

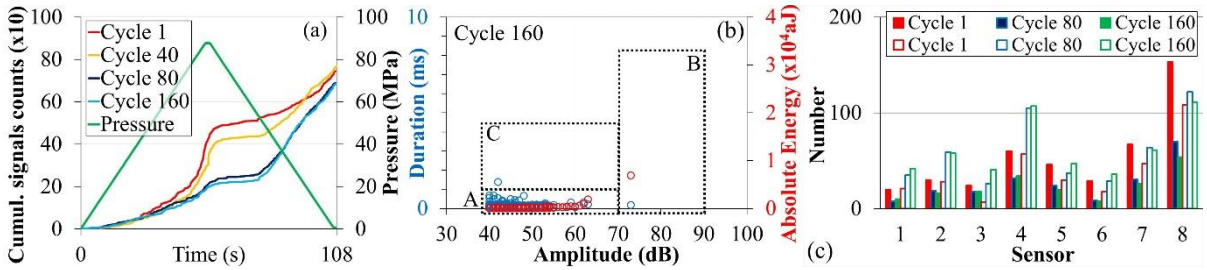

Figure 11: (a) Cumulative AE signals counts and pressure versus time – (b) Acoustic response of the duration and absolute energy of AE signals as a function of amplitude (Cycle 160) – (c) Number of type A signals per channel for the three cycles 1, 80 and 160 when Load (full square) and Unload (hollow square)

5 Conclusion

In this study, a test on a type IV tank by coupling acoustic emission with a non-contact optical measurement method has been performed to complete the knowledge on the behavior of structures for correlation with numerical simulation. The coupling of the two optical and acoustic measurement methods provides different but perfectly complementary information. The method of measuring the displacement (and strain) field on the surface of the tank allows a perfect knowledge of its kinetics during a complex loading over time (cycling test). This macro behavior can be correlated with the response of the structure (composite shell) captured by the acoustic emission technique. All the tests carried out show the interest in using these two types of measurements simultaneously. Although displacements (and strains) are small and reversible, the stereoscopic marker tracking technique shows its reliability in obtaining

reproducible measurements on a complex structure (cylindrical tank) and permits to discern some fluctuations. The mechanism measured in all the tests via acoustic emission corresponds to friction or stick-lick. Under the chosen test conditions (maximum pressure of 87.5MPa), the linear and reversible behavior of the structure (small strains) can therefore only be related here to the internal friction perceived by the acoustic emission. This validation of feasibility at small deformations makes it seem conceivable that, at higher pressures, it would be possible to link the mechanical behavior of the tank with the appearance and propagation of the damage in the composite layer.

Finally, the test/simulation correlation shows that with this test and the associated optical metrology it is quite possible to identify a behavioral model. This identification could be done by a complete characterization of the composite by tests on specimens (classical). But it could also be done by inverse problem using the experimental results of the different tests used in this article.

Acknowledgments

This work was partially funded by the French Government program "Investissements d'Avenir" (EQUIPEX GAP, reference ANR-11-EQPX-0018). This work was supported by the CPER-FEDER project of Region Nouvelle Aquitaine CPER-FEDER NeoFac (convention P-2016-BAFE-12). The reservoir used was built in part thanks to funding from the National Research Agency (ANR) in the project Colline - http://www.agence-nationale-recherche.fr/?Project=ANR-13-RMNP-0007.

References

[1] Barthelemy H, Weber M, Barbier F. Hydrogen storage: recent improvements and industrial perspectives. Int J Hydrogen Energy. 2017; 42:7254-62. https://doi.org/10.1016/j.ijhydene.2016.03.178

[2] Berro Ramirez JP, Halm D, Grandidier J-C, Villalonga S, Nony F. 700 bar type IV high pressure hydrogen storage vessel burst – Simulation and experimental validation. Int J Hydrogen Energy 2015;40:13183-92. https://doi.org/10.1016/j.ijhydene.2015.05.126.

[3] Gentilleau B, Bertin M, Touchard F, Grandidier J-C. Stress analysis in specimens made of multi-layer polymer/composite used for hydrogen storage application: comparison with experimental results. Composite structures 2011;93(11): 2760-2767. https://doi.org/10.1016/j.compstruct.2011.05.028

[4] Gentilleau B, Touchard F, Grandidier J-C. Numerical study of influence of temperature and matrix cracking on type IV hydrogen high pressure storage vessel behavior. Composite Structures 2014;11:98-110. https://doi.org/10.1016/j.compstruct.2013.12.034

[5] Gentilleau B, Touchard F, Grandidier J-C, Mellier D. Numerical Determination and Experimental Validation of a Technological Specimen Representative of High-Pressure Hydrogen Storage Vessels. Mechanics of Composite Materials 2015;51:465-478. https://doi.org/10.1007/s11029-015-9518-3

[6] Berro Ramirez JP, Halm D, Grandidier J-C, Villalonga S, Nony F. Experimental study of the thermomechanical behavior of wound notched structures. Int J Hydrogen Energy 2015;40:13148-159. https://doi.org/10.1016/j.ijhydene.2015.05.156

[7] Bertin M, Touchard F, Lafarie-Frenot M-C. Experimental study of the stacking sequence effect on polymer/composite multi-layers submitted to thermomechanical cyclic loadings. Int J Hydrogen Energy 2010;35:11397-404. https://doi.org/10.1016/j.ijhydene.2010.07.018
[8] Berro Ramirez JP, Halm D, Grandidier J-C, Villalonga S. A fixed directions damage model for composite materials dedicated to hyperbaric type IV hydrogen storage vessel – Part I: Model formulation and identification. Int J Hydrogen Energy 2015;40:13165-173. https://doi.org/10.1016/j.ijhydene.2014.08.071
[9] Berro Ramirez JP, Halm D, Grandidier J-C, Villalonga S. A fixed directions damage model for composite materials dedicated to hyperbaric type IV hydrogen storage vessel – Part II: Validation on notched structures. Int J Hydrogen Energy 2015;40:13174-82. https://doi.org/10.1016/j.ijhydene.2015.06.014
[10] Berro Ramirez JP, Halm D, Grandidier J-C. Assessment of a damage model for wound composite structures by acoustic emission. Composite Structures 2019;214:414-421. https://doi.org/10.1016/j.compstruct.2019.01.093
[11] Magneville B, Gentilleau B, Villalonga S, Nony F, Galiano H. Modeling, parameters identification and experimental validation of composite materials behavior law used in 700bar type IV hydrogen high pressure storage vessel. Int J Hydrogen Energy 2015;40:13193-205. https://doi.org/10.1016/j.ijhydene.2015.06.121.
[12] Benelfellah A, Quach T, Halm D, Rogaume T, Bertheau D. Characterization and modelling of composite material behavior submitted previously to fire exposure. In: Proc. 20th international conference on composite materials, Copenhague, Denmark; 2015.
[13] Pepin J, Lainé E, Grandidier J-C, Benoit G, Mellier D, Weber M, Langlois C. Replication of liner collapse phenomenon observed in hyperbaric type IV hydrogen storage vessel by explosive decompression experiments. Int J Hydrogen Energy 2018;43:4671-80. https://doi.org/10.1016/j.ijhydene.2018.01.022.
[14] Pepin J, Lainé E, Grandidier J-C, Benoit G, Blanc-Vannet P, Weber M. Determination of key parameters responsible for polymeric liner collapse in hyperbaric type IV hydrogen storage vessel. Int J Hydrogen Energy 2018;43:16386-99. https://doi.org/10.1016/j.ijhydene.2018.06.177
[15] Bie H, Li X, Liu P, Liu Y, Xu P. Fatigue life evaluation of high pressure hydrogen storage vessel. Int J Hydrogen Energy 2008;35:2633-36.
[16] Halm D, Fouillen F, Lainé E, Gueguen M, Bertheau D, vanEekelen T. Composite pressure vessels for hydrogen storage in fire conditions: fire tests and burst simulation. Int J Hydrogen Energy 2017;42:20056-70. https://doi.org/10.1016/j.ijhydene.2017.06.088.
[17] Blanc-Vannet P, Papin P, Weber M, Renault P, Pepin J, Lainé E, Tantchou G, Castagnet S, Grandidier J-C. Sample scale testing method to prevent collapse of plastic liners in composite pressure vessels. Int J Hydrogen Energy (Special Issue ICHS 2017) 2019;44:8682-91. https://doi.org/10.1016/j.ijhydene.2018.10.031
[18] Knapp RH, Robertson IN. Fiber optic sensor system for filament-wound pressure vessels, Proceedings of the Inter-national Offshore and Polar Engineering Conference (2000)77–82.
[19] Degrieck J, Waele WD. Embedded optical Bragg-sensors for monitoring of filament wound pressure vessels. European J of Mechanical and Environmental Engineering 1999;44:205-214.

[20] Walker JL, Russell SS, Workman GL, Hills EK. Neural network/acoustic emission burst pressure prediction for impact damaged composite pressure vessels. Materials Evaluation 1997;55:903-907.
[21] Yao XF, Meng LB, Jin JC, Yeh HY. Full-field deformation measurement of fiber composite pressure vessel using digital speckle correlation method. Polymer testing 2005;24:245-251.
[22] Meng LB, Jin JC, Yao XF, Yeh HY. 3D Full-field deformation monitoring of fiber composite pressure vessel using 3D digital speckle correlation method. Polymer testing 2006;25:42-48.
[23] Gąsior P, Malesab M, Kaletaa J, Kujawińskab M, Malowanyb K, Rybczyńskia R. Application of complementary optical methods for strain investigation in composite high pressure vessel. Composites Structures 2018;203:718-734. https://doi.org/10.1016/j.compstruct.2018.07.060
[24] Kwon JR, Lyu GJ, Lee TH, Kim JY. Acoustic emission testing of repaired storage tank. Int J Pressure Vessels and Pipping 2001;78:373-378. https://doi.org/10.1016/S0308-0161(01)00038-2
[25] Lin S, Jia X, Sun H, Sun H, Hui D, Yang X. Thermo-mechanicalproperties of filament wound CFRP vessel under hydraulic andatmospheric fatigue cycling. Compos Part B 2013;46:227-33.
[26] Chou HY, Mouritz AP, Bannister MK, Bunsell AR. Acoustic emission analysis of composite pressure vessels under constant and cyclic pressure. Composites: Part A 2015;70:111-120. DOI: 10.1016/j.compositesa.2014.11.027
[27] Dahmene F, Yaacoubi S, Mountassir ME, Langlois C, Barboux O. Towards efficient acoustic emission testing of COPV, without Felicity ratio criterion, during hydrogen-filling. Int J Hydrogen Energy 2016;41:1359-68. https://doi.org/10.1016/j.ijhydene.2015.11.065
[28] Liao BB, Wang DL, Hamdi M., Zheng JY, Jiang P, Gu CH, Hong WR. Acoustic emission-based damage characterization of 70MPa type IV hydrogen composite pressure vessels during hydraulic tests. Int J Hydrogen Energy 2019;44:22494-506. https://doi.org/10.1016/j.ijhydene.2019.02.217
[29] Brémand F, Cottron M, Doumalin P, Dupré J-C, Germaneau A, Valle V. Mesures en mécanique par méthodes optiques. Techniques de l'ingénieur, 2. R1850, 2011.
[30] Dupré J-C, Doumalin P, Husseini HA, Germaneau A et al. Displacement Discontinuity or Complex Shape of Sample: Assessment of Accuracy and Adaptation of Local DIC Approach. Strain 2015;51:391–404. https://doi.org/10.1111/str.12150
[31] Bretagne N, Valle V, Dupré J-C. Recent developments of the mark tracking technique: application to strain field and volume variation measurements. NDT & E International 2005;38:290-298. https://doi.org/10.1016/j.ndteint.2004.09.003
[32] Germaneau A, Doumalin P, Dupré J-C, Brèque C, Brémand F, D'Houtaud S, Rigoard P. Experimental analysis of mechanical response of stabilized occipitocervical junction by 3D mark tracking technique, European Physical Journal, 14th International Conference on Experimental Mechanics, Poitiers (France),. EPJ Web of Conferences 6, 21004 (2010).
[33] Malpot A. Etude du comportement en fatigue d'un composite à matrice polyamide renforcé d'un tissue de fibres de verre pour application automobile. Ph.D thesis, ISAE-ENSMA (Poitiers), 2017. https://tel.archives-ouvertes.fr/tel-01505589

[34] Huguet S, Godin N, Geartener R, Salmon L, Villard D. Use acoustic emission to identify damage modes in glass fibre reinforced polyester. Composites Science and Technology 2002;62:1433-1444. https://doi.org/10.1016/S0266-3538(02)00087-8
[35] Nechad H. Evaluation de l'endommagement et de la rupture de matériaux hétérogènes par ultrasons et émission acoustique : Estimation de la durée de vie restante. Ph.D thesis, INSA de Lyon, 2004.
[36] NF EN 12245 : 2009. Bouteilles à gaz transportables, Bouteilles entièrement bobinées en matériaux composites.
[37] Nielsen A. Acoustic Emission Source based on Pencil Lead Breaking. The Danish Welding Institute Publication 1980;80:15-20.
[38] Jemielniak K. Some aspects of acoustic emission signal pre-processing. J Mat Proc Tech 2001;109:242-247. https://doi.org/10.1016/S0924-0136(00)00805-0
[39] Tung Pham T. Caractérisation expérimentale et numérique de la dégradation des réservoirs hyperbares en composite bobiné soumis à des chocs. Ph.D thesis, ISAE-ENSMA (Poitiers), 2013. https://tel.archives-ouvertes.fr/tel-00941534
[40] Peters ST. Composite filament winding. ASM International; 2011.
[41] Leh D, Saffré P, Francescato P, Arrieux R. Multi-sequence dome lay-up simulations for hydrogen hyper-bar composite pressure vessels. Compos Part A 2013;52:106-117. https://doi.org/10.1016/j.compositesa.2013.05.007